Title

Super water absorbing and shape memory nanocellulose aerogels from TEMPO-oxidized cellulose nanofibrils via cyclic freezing–thawing

Permalink

https://escholarship.org/uc/item/8867r30z

Journal

Journal of Materials Chemistry A, 2(2)

ISSN

2050-7488

Authors

Jiang, Feng
Hsieh, You-Lo

Publication Date

2014

DOI

10.1039/c3ta13629a

Peer reviewed

Journal of
Materials Chemistry A

PAPER

View Article Online
View Journal | View Issue

Cite this: *J. Mater. Chem. A*, 2014, **2**, 350

Super water absorbing and shape memory nanocellulose aerogels from TEMPO-oxidized cellulose nanofibrils *via* cyclic freezing–thawing†

Feng Jiang and You-Lo Hsieh*

Received 10th September 2013
Accepted 28th October 2013

DOI: 10.1039/c3ta13629a

www.rsc.org/MaterialsA

Mechanically robust cellulose nanofibril (CNF) aerogels with ultralow density (8 mg cm^{-3}), superior porosity (99.5%), super water absorbency (104 g g^{-1} water/dried mass), high crystallinity (68.5%) as well as exceptional wet resilience and water activated shape recovery were facilely fabricated for the first time by ice-crystal templated self-assembly of TEMPO oxidized CNFs *via* cyclic freezing–thawing. With ultrathin widths (1–2 nm), high aspect ratios (several hundreds) and numerous surface polar hydroxyls and carboxyls, TEMPO oxidized CNFs behaved similar to aqueous soluble polymers to form strong freestanding hydrogels by repetitive freezing (−20 °C, 15 h) and thawing (room temperature, 9 h). The spaces occupied by the several hundred microns wide ice crystals were well preserved upon freeze-drying, deriving macroporous CNF aerogels with over 99% porosity of interconnected pores. The freezing induced self-assembling of CNFs was observed at a low concentration of 0.05%, whilst more ordered macroporous honeycomb structures were observed at and above 0.2%. Exchanging water in the CNF hydrogel with *tert*-butanol generated hierarchical CNF aerogels containing several hundred microns sized macroscopic as well as mesoscopic pores ranging from 2 to 90 nm with further improved specific surface area (117.8 m^2 g^{-1}), pore volume (1.19 cm^3 g^{-1}) and water absorption (116 g g^{-1}). All CNF aerogels demonstrated super water absorbency, fast water-activated shape recovery in 4 s and reusability for at least 20 times.

Introduction

Aerogels are ultra-lightweight and highly porous materials typically derived from wet gels of inorganic oxides by supercritical or freeze drying.[1] With very low thermal conductivity as well as unique optical and acoustic properties, the most common silica aerogels have found wide ranging applications as sensors, detectors, drug carriers, thermal and acoustic insulations as well as absorbents.[2] Inorganic aerogels, however, suffer from inherent friability that limits their applications where mechanical strength is required. More mechanically robust aerogels have been derived from organic materials, such as the most common resorcinol-formaldehyde (RF) aerogels.[3] Recently, aerogels with over 90% compressive strain[4] and impact strength of 10 times that of RF aerogels[5] have been fabricated from cellulose[6–8] for magnetic,[9] electrical conductive,[7] hydrophobic and oleophobic,[10,11] and absorbent[12–14] applications as well as supports for inorganic nanomaterials.[15–17]

Cellulose aerogels can be fabricated from either homogeneous cellulose solutions[18–25] or heterogeneous aqueous nanocellulose suspensions.[4,7,11,13,26–34] Aerogels prepared from cellulose solutions require lengthy, multiple steps of dissolving cellulose in solvents, such as alkali hydroxide/urea solution,[18] calcium thiocyanate tetrahydrate,[19] *N*-methyl-morpholine-*N*-oxide,[20,21] sodium hydroxide,[22] lithium chloride/dimethylacetamine,[23] lithium chloride/dimethyl sulfoxide[24] and ionic liquid,[25] followed by induced gelation, solvent exchange and supercritical or freeze drying. Aerogels from dissolved cellulose had a specific surface area as high as 404 m^2 g^{-1},[17] less than half of that of the typical silica aerogels (over 1000 m^2 g^{-1}),[35] and densities ranging from 20–200 mg cm^{-3},[19,20,22] one to two orders of magnitude higher than those of the silica aerogel (2–3 mg cm^{-3}).[36] Instead of the amorphous or cellulose II structure from dissolution,[18,23] supercritical or freeze drying of aqueous nanocellulose suspensions has the advantage of retaining the native cellulose Iβ crystalline structure.[30–32] These nanocellulose aerogels have similar specific surface areas (10–284 m^2 g^{-1}),[4,28] but lower densities (0.27–103 mg cm^{-3})[4,7,11,13] than those from cellulose solutions. Nanocellulose aerogels, however, easily disintegrate in water[29,34] and require chemical[29] and cationic[37] crosslinking or physical gelation by ultrasound energy,[30,32] solvent exchange[38] and reduced electrostatic repulsion *via* protonation of surface charge groups[26] to improve wet

---

Fiber and Polymer Science, University of California, Davis, CA 95616, USA. E-mail: ylhsieh@ucdavis.edu; Fax: +1 530 752 7584; Tel: +1 530 752 0843

† Electronic supplementary information (ESI) available: Picture of the 0.5 FT CNF aerogel cut into various shapes; 3 FT hydrogel handled by hand; more SEM images. See DOI: 10.1039/c3ta13629a

strength. These additional crosslinking and gelation processes demand extra chemical and energy inputs.

Freezing and thawing of aqueous poly(vinyl alcohol) (PVA) has shown to induce physical crosslinked hydrogels.[39] Cyclic freezing–thawing of PVA[40] and starch/PVA[41] solutions containing cellulose nanocrystals also yielded hydrogels. Furthermore, freezing and thawing of wood flour dissolved in ionic liquids followed by supercritical CO_2 drying produced low density (150 mg cm^{-3}), high porosity (97%)[42] and modest specific surface area (80 m^2 g^{-1})[43] lignocellulose aerogels. Gelation of nanocellulose suspensions alone *via* freezing–thawing has not been reported.

This work explored the gelation of aqueous colloidal suspensions of nanometer wide, high aspect ratio cellulose nanofibrils (CNFs) by cyclic freezing–thawing and their freeze drying toward formation of highly crystalline cellulose Iβ aerogels. Approximately 2 nm wide and 1 μm long CNFs were robustly derived from pure rice straw cellulose by TEMPO (2,2,6,6-tetramethylpyperidine-1-oxyl) oxidation coupled with mechanical defibrillation at 96.8% yield.[31] With numerous surface hydroxyls and carboxyls, as well as lateral dimensions and high aspect ratios approaching macromolecules, aqueous CNF suspensions were hypothesized to gel similar to PVA by the freezing–thawing process. How cyclic freezing–thawing as well as *tert*-butanol (TBA) exchange affect hydrogel formation and structures of aerogels from freeze drying was investigated in terms of the porous structure, density, porosity, water absorption capacity, crystallinity, specific surface area, pore size distribution and reusability.

Experimental section

Materials

Pure cellulose was isolated from rice straw (Calrose variety) following a previously reported process to a 36% yield.[34] CNFs were isolated from pure rice straw cellulose employing 5 mmol NaClO per gram of cellulose and mechanical blending at 37 000 rpm for 30 min. Sodium hypochlorite solution (NaClO, 11.9%, reagent grade, Sigma-Aldrich), 2,2,6,6-tetramethylpyperidine-1-oxyl (TEMPO, 99.9%, Sigma-Aldrich), sodium bromide (NaBr, BioXtra, 99.6%, Sigma-Aldrich), *tert*-butanol (certified, Fisher Scientific), and Procion Red MX-5B (dye content 40%, Sigma-Aldrich) were used as received without further purification. All water used was purified using a Milli-Q plus water purification system (Millipore Corporate, Billerica, MA).

Preparation of CNF aerogels

CNF aerogels were prepared by freezing alone or cyclic freezing–thawing (FT) of CNF suspensions of varied % concentrations by weight unless specified otherwise. Either freezing alone or cyclic FT of 10 mL 0.6% CNF suspensions was performed in a glass centrifuge tube, followed by freeze-drying. Freezing alone was conducted at either −20 °C in a freezer for 15 h or −196 °C in liquid nitrogen for 10 min, followed by freeze-drying at −50 °C for 2 days. It should be noted that the CNF suspensions were frozen in approximately 2 h at −20 °C and 5 min in liquid nitrogen. Thus shorter freezing times were possible, making the process more energy and time efficient. Cyclic freezing–thawing of the CNF suspension (0.6%) involved freezing at −20 °C for 15 h and thawing at ambient temperature for 9 h as one FT cycle. Thawed samples at the end of 1, 3, 5 and 7 FT cycles were quickly frozen in liquid nitrogen and then freeze-dried into CNF aerogels and referred to as the *x* FT aerogel, with *x* standing for the number of FT cycles. The thawed 1 FT hydrogel was also frozen at −20 °C for 15 h and then freeze-dried, yielding 1.5 FT aerogels. The thawed 3 FT hydrogel was placed into *tert*-butanol to exchange water to *tert*-butanol for 12 h thrice, and then freeze-dried, as termed as 3 FTTBA. Cellulose nanofibril suspensions at lower concentrations of 0.05, 0.1, 0.2 and 0.4% were subjected to 3 FT cycles following the same procedure, followed by liquid nitrogen freezing and freeze-drying, in order to study the effects of concentration on the aerogel morphologies.

Density, porosity and water absorption capacity of CNF aerogels

Each cylindrical CNF aerogel was cut to approximately 10 mm long sections. The dimensions (length and diameter) and mass were measured using a digital caliper and balance to 0.01 mm and 0.1 mg resolution, respectively, to calculate the aerogel density (ρ_a). The porosity of aerogel was calculated as:

$$\text{Porosity (\%)} = \left(1 - \frac{\rho_a}{\rho_c}\right) \times 100\% \tag{1}$$

where ρ_c is the bulk density of cellulose taken as 1600 mg cm^{-3}.[44]

The ability of aerogels to absorb water was measured by immersing 10 mm long cylindrical aerogels in 20 mL water and allowed to saturate. After blotting the surface water on saturated gels with filter paper, the saturated aerogel was weighed. The water absorption capacity (g g^{-1}) of CNF aerogels was measured and calculated as:

$$\text{Measured water absorption capacity} = \frac{(w_e - w_o)}{w_o} \tag{2}$$

where w_e and w_o are weights of fully water saturated and dry aerogels, respectively.

The water absorption capacity of aerogels was also calculated based on the unchanged overall volume of water saturated aerogels:

$$\text{Calculated water absorption capacity} = \frac{\text{Porosity} \times \rho_{\text{water}}}{\rho_a} \tag{3}$$

where ρ_{water} is the density of water at 20 °C taken as 0.9982 g cm^{-3}.[45]

Scanning electron microscopy (SEM)

Each CNF aerogel was cryosectioned by cutting liquid nitrogen frozen aerogels using a sharp razor, in radial cross-sections (at right angle to axis) and longitudinal sections (through the axis) of the cylinder, to visualize both the internal and external surface (next to the glass tube inner wall) morphologies. Samples were mounted with conductive carbon tape, sputter coated with gold and imaged using a field emission scanning electron microscope (FE-SEM) (XL 30-SFEG, FEI/Philips, USA) at a 5 mm working distance and a 5 kV accelerating voltage.

BET specific surface area

The specific surface area and pore characteristics of CNF aerogels were determined by N_2 adsorption at 77 K using a surface area and porosity analyzer (ASAP 2000, Micromeritics, USA). Approximately 0.055 g of each sample was degassed at 35 °C for 24 h. The specific surface area was determined by the Brunauer–Emmett–Teller (BET) method from the linear region of the isotherms in the 0.06–0.20 relative P/P_0 pressure range. Pore size distributions were derived from the desorption branch of the isotherms by the Barrett–Joyner–Halenda (BJH) method. The total pore volumes were estimated from the amount adsorbed at a relative pressure of $P/P_0 = 0.98$.

X-ray diffraction and crystallinity

The XRD spectra of CNF aerogels were collected on a Scintag XDS 2000 powder diffractometer using a Ni-filtered Cu Kα radiation ($\lambda = 1.5406$ Å) at an anode voltage of 45 kV and a current of 40 mA. Aerogels with 5 mm thickness were compressed between two glass slides into 1 mm thickness. Diffractograms were recorded from 5° to 40° at a scan rate of 2° per min. The crystallinity index (CrI) was calculated from the intensity of the 200 peak (I_{200}, $2\theta = 22.6°$) and the intensity minimum between 200 and 110 (I_{am}, $2\theta = 18.7°$) peaks using the empirical equation:[46]

$$\mathrm{CrI} = \frac{I_{200} - I_{\mathrm{am}}}{I_{200}} \times 100 \tag{4}$$

Results and discussion

Freezing temperatures on CNF aerogels

Cellulose nanofibrils (CNFs) with an average width of 2.1 (±0.4) nm and lengths of up to 1 μm were prepared *via* coupled TEMPO mediated oxidation and mechanical blending to a 96.8% yield.[47] The primary C6 hydroxyls on these CNF surfaces were 70.9% converted to carboxyls at 1.29 mmol g^{-1} of CNFs, providing electrostatic repulsions for stable aqueous suspensions. Aqueous CNF suspensions at 0.6% were frozen at either −196 °C for 10 minutes or −20 °C for 15 h, then freeze-dried to white aerogels (insets, Fig. 1a & d). Both aerogels had similarly low densities of 8.0 mg cm^{-3} and a very high porosity of 99.5%. While both aerogels were super water-absorbing and showed no dimensional change when fully water saturated, the one frozen at −20 °C absorbed much more water (104 g of water per gram of dried aerogel) than that frozen at −196 °C (37 g g^{-1}). The aerogel frozen at −20 °C also stayed intact as one cylindrical piece, shaped by the glass tube (inset, Fig. 1a), and could be easily cut into different shapes (thin disc, square, wedge, trapezoid, *etc.*) using a sharp razor without appreciable deformation (Fig. S1, ESI†). The aerogel frozen at −196 °C, on the other hand, was weak in structure, falling apart when handled using a pair of forceps (inset, Fig. 1d). Both aerogels showed irregularly shaped pores framed by film-like walls of assembled CNFs, but with distinctly different pore sizes and pore wall textures (Fig. 1). The radial cross-section of the aerogel frozen at −20 °C showed significantly larger pores of several hundred microns wide with ultra thin and smooth walls (Fig. 1a) while much smaller pores of tens of microns wide surrounded by irregularly corrugated and thicker walls were observed on that frozen at −196 °C (Fig. 1d). The aerogels frozen at −20 °C showed isotropic pore morphologies, *i.e.* similar macro-scale pores in both longitudinal and radial cross-sections (Fig. 1b). In contrast, aerogels frozen at −196 °C had a clearly anisotropic pore morphology (Fig. 1e), showing pore walls aligned more along the longitudinal than the radial cross-sections. The external surfaces of both cylindrically shaped aerogels were similarly rough with some open pores (Fig. 1c & f), containing films with imbedded micro-fibrils that are more prominent in the aerogel frozen at −196 °C. In contrast to the continuous surface of the aerogel frozen at −20 °C (inset, Fig. 1c), the surface of the aerogel frozen at −196 °C contained hundreds of micrometers long inter-connecting surface cracks, to which its easy disintegration is attributed (inset, Fig. 1f).

The distinction between these aerogels, in both pore morphology and physical integrity, is primarily attributed to the manner in which CNFs associate in response to the freezing rates in which water is frozen at these temperatures. During freezing, the aqueous suspension becomes super-cooled before ice nucleates and propagates, with the degree of super-cooling ahead of the freezing front positively related to the cooling rate. As noted earlier, the CNF suspension was frozen in 2 h at −20 °C whereas freezing occurred in minutes at −196 °C, thus the super-cooling rate at −196 °C was much faster than that at −20 °C. Based on the inverse relationship between the ice nuclei sizes and the degree of super-cooling,[48] much smaller nuclei are expected with faster super-cooling at −196 °C. The observed pore sizes, from sublimation of ice in freeze drying, are consistent with the numerous, much smaller ice nuclei grown under faster super-cooling and rapid nucleation at −196 °C. The slower super-cooling and ice nucleation at −20 °C allow ice crystals to grow in sizes. Judging by the pore sizes, ice crystals formed at −20 °C are more than 20 times of those formed at −196 °C. Other than pore sizes, the morphological difference of pore walls also shows the effects of the freezing temperatures or the rate of ice formation on the organization of CNFs. Upon ice nucleation, the well-dispersed CNF suspension turns into CNF rich domains surrounding the ice crystals. As ice crystals grow slowly and larger at −20 °C, more CNFs are excluded and concentrated to assemble into more ordered structures, forming smoother organized domains around larger crystals that, upon sublimation, become pores. In contrast, CNFs are more dispersed among rapidly nucleated, smaller ice crystals at a much lower freezing temperature of −196 °C, resulting in much smaller pores and thinner walls of less organized CNFs. The better physical integrity of the aerogel from freezing at −20 °C is attributed to its thicker and more organized pore walls.

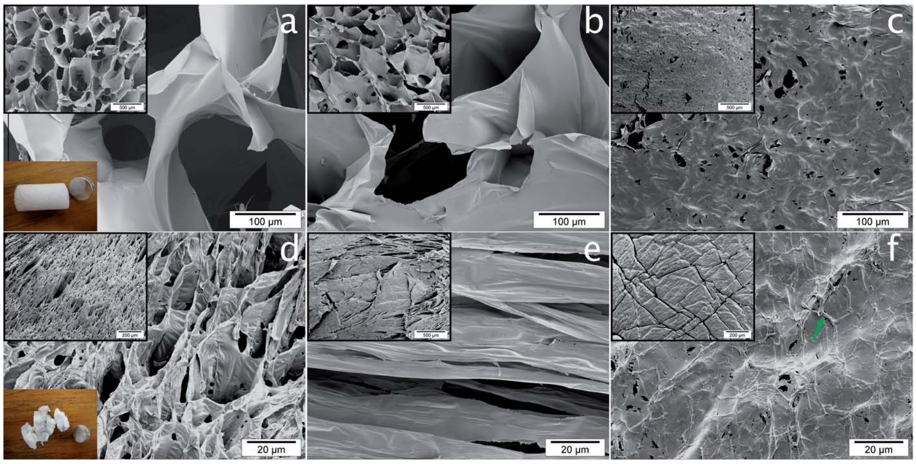

Fig. 1 CNF aerogels from freezing 0.6% CNF suspensions at −20 °C (a–c) and −196 °C (d–f) followed by freeze drying: (a and d) radial cross-sections, lower left insets are photographs of aerogels; (b and e) longitudinal sections; (c and f) external surfaces. The arrow in (f) points to one of many microfibrils on the surface. Inset scale bar = 500 μm (a, b, c and e) and 200 μm (d and f).

Cyclic freezing–thawing on CNF hydrogels and aerogels

The above observation affirms freezing or the ice nucleation rate in CNF suspensions to be the driving force for CNF association. The isotropic morphology and strong physical integrity of the aerogel from freezing at −20 °C gave clear evidence of better-organized CNF structures. To observe gelation and network formation, a −20 °C freezing temperature was used in cyclic freezing–thawing of CNF suspensions. At 0.6%, the aqueous CNF suspension appeared as a viscous fluid, flowing freely with gravity in an inverted tube (Fig. 2a). After freezing at −20 °C for 15 h then thawing at ambient temperature for 9 h, or 1 FT cycle, the viscous CNF suspension became a firm gel and remained at the bottom of the inverted tube (Fig. 2b). After 3 FT cycles, some free water was excluded and allowed the hydrogel to fall in an inverted tube (Fig. 2c). Upon removing from the tube, the CNF hydrogel retained its same tubular shape (Fig. 2d) and could be handled by hand easily while holding all the trapped water and its own weight (Fig. S2, ESI†). After freeze-drying, the CNF hydrogel became a super light aerogel with no appreciable change in dimensions (Fig. 2e). To reaffirm the earlier observation, the 0.6% CNF suspension was frozen at −196 °C (10 min) and similarly thawed (ambient temperature, 9 h). Gelation was not observed after one or repetitive cycles, due to the much lesser extent of assembled CNFs from the faster ice nucleation as discussed in the previous section.

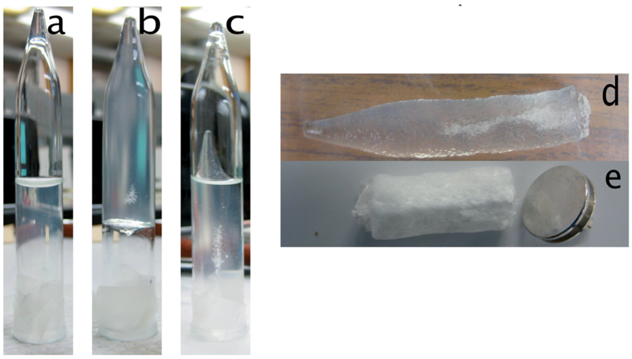

Fig. 2 Photographs of 0.6% CNF: (a) suspension; (b) hydrogel after 1 FT cycle; (c & d) hydrogel after 3 FT cycles; (e) freeze-dried aerogel after 3 FT cycles.

The individual effects of freezing and thawing on the morphological development of CNF aerogels were further investigated. The aerogel from freezing at −20 °C then freeze-dried, *i.e.* without thawing as shown earlier, was re-designated as the 0.5 FT aerogel, and showed smooth pore wall surfaces and interconnected hundreds of microns sized pore structures (Fig. 1a & b). The 1 FT aerogel from freezing at −20 °C and thawing at room temperature for 9 h, then frozen at −196 °C and freeze dried, contained irregularly shaped pores in both directions with fibrillar networks (Fig. 3a & b). The irregular, thin fibers attached pore walls and smaller pores of the 1 FT aerogel differed significantly from the ordered, larger pores with smooth pore walls of the 0.5 FT aerogel. Also, the 1 FT aerogel had porous external surfaces (Fig. 3c) with pores smaller than those in either radial cross or longitudinal sections (Fig. 3a and b) and in contrast to the smooth and mostly closed surface of the 0.5 FT aerogel (Fig. 1c). After freezing the 1 FT CNF hydrogel at −20 °C for another 15 h then freeze-dried, the 1.5 FT aerogel showed more ordered and larger interconnected pores framed by smooth pore walls (Fig. 3d & e), similar to the 0.5 FT aerogel, whereas the external surface became rougher containing larger and more irregular pores than that of the 0.5 FT aerogel (Fig. 3f). After 3 FT cycles, the aerogel had more ordered and closely packed honeycomb structures with *ca.* 100 μm pores (Fig. 3g) with elongated tubular shaped pores along the longitudinal direction (Fig. 3h), showing a more anisotropic pore structure. Similar to the 1 FT aerogel, the surface of the 3 FT aerogel also contained numerous open pores that are much smaller than those of the 1.5 FT aerogel (Fig. 3i). With increasing FT cycles, the 5 and 7 FT aerogels became smaller in dimensions and had smaller pores and less porous surfaces (Fig. S3, ESI†), as well as less thin fibers attached to the pore walls, indicating progressively enhanced assembling with increased FT cycles.

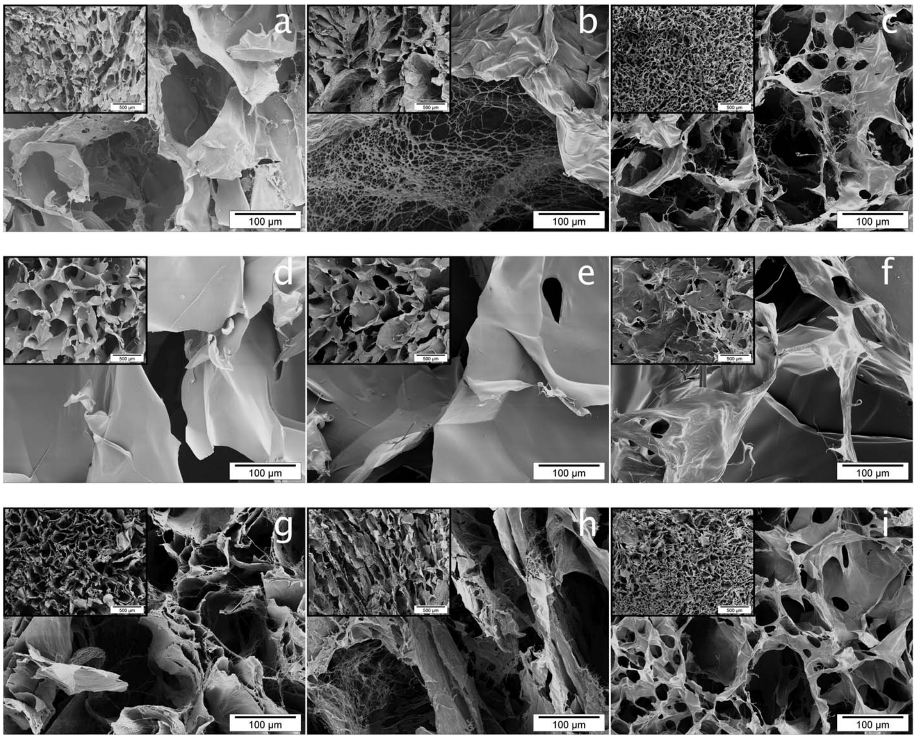

Fig. 3 Aerogels from 1 (a–c), 1.5 (d–f) and 3 (g–i) FT cycles of 0.6% CNF suspension: (a, d, and g) radial cross-sections; (b, e, and h) longitudinal section; (c, f, and i) external surfaces. Inset scale bar = 500 μm.

In freezing dilute CNF suspensions, CNFs assemble into circumambient thin films templated around the ice crystals. The observed evolution of pore morphology confirms that ice crystal formation as a result of freezing temperatures or freezing rates prior to freeze-drying is pivotal in defining the aerogel microstructures. Freezing at −20 °C prior to freeze-drying forms larger ice crystals and concentrates more CNFs in between, leading to larger pores surrounded by better organized and thicker assembled CNF walls (as in 0.5 and 1.5 FT aerogels). Thawing offers the opportunity for assembled and un-associated CNFs to rearrange. As ice crystals melt in thawing, surface CNFs and those not closely associated with each other in previous freezing regain mobility and tend to reassemble and organize into thin fibers by rapid −196 °C freezing (as in 1 and 3 FT aerogels). For aerogels frozen at −196 °C prior to freeze-drying, progressive assembling of CNFs is observed with increasing FT cycles (as seen in 1, 3, 5, and 7 FT aerogels), resulting in more extensively assembled and thicker films, as well as less unassembled thin fibers.

Applying freezing–thawing to CNF suspensions at lower concentration of 0.4, 0.2, 0.1 and 0.05% also induced CNF assembly into hydrogels and aerogels at 3 FT cycles, however into more contracted overall volumes with lowering CNF concentrations. Highly irregularly shaped pores interspersed with numerous ultra-thin fibers were observed in aerogels from the two lowest concentrations (0.05 and 0.1%) while a more ordered elongated porous structure emerged at 0.2%, then an even more ordered mix of isotropic and elongated pores at 0.4% (Fig. 4), and finally to more uniform honeycomb patterned pores at 0.6% (Fig. 3g). The pore sizes of aerogels from a CNF concentration of 0.2% and above are in similar 100 μm ranges, suggesting that the pore sizes are primarily defined by the size of ice crystals. At 0.05 and 0.1% CNF concentrations, the overall aerogel surfaces were also more fibrous whereas those from above 0.2% were more film-like (Fig. S4 in the ESI†). The morphologies of assembled nanocellulose during freeze-drying are greatly affected by the suspension concentrations, transitioning from fiber to film with increasing nanocellulose

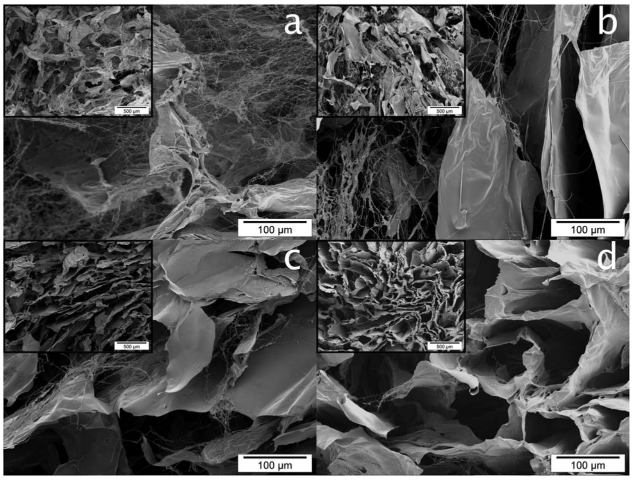

Fig. 4 Radial cross-sections of 3 FT aerogels of aqueous CNF suspensions at: (a) 0.05%; (b) 0.1%; (c) 0.2% and (d) 0.4% concentrations. Inset scale bar = 500 μm.

concentrations.[32,49] As discussed previously, freezing and freeze-drying induced assembly of nanocellulose is primarily through ice-crystal formation that excludes and concentrates the nanocellulose in between leading to a concentrated nanocellulose rich phase. In the nanocellulose rich phase, cellulose nanofibrils are in close proximity to each other to associate and are assembled into macroscopic scale domains. At lower concentrations of 0.05 and 0.1%, the scarcity of CNFs caused them to assemble into very fine fibers and thin films. As the CNF concentration increases to 0.2 and 0.4%, ice templating led the significantly more numerous CNFs to assemble into all types of films and thicker films. The threshold CNF concentration was 2%, above which CNFs can assemble into thin films that encase cellular pore structures that contained little unassembled thin fibers.

Aerogel structures and properties

The effects of cyclic freezing–thawing and freeze drying were further examined in respect of the aerogel density, porosity, water absorption capacity, specific surface area and crystallinity. For consistency, the aerogel from freezing at −196 °C and freeze-dried was re-designated as the 0 FT aerogel, *i.e.* not subject to freezing–thawing. From 0.6% initial CNF concentration, the lowest density achieved was around 8.0 mg cm^{-3} with 1 FT cycle or less (0 and 0.5 FT). Consistent with previously observed increasing CNF assembly with increasing FT cycles, the aerogel density increased to 11.6, 12.9 and 18.7 mg cm^{-3} after 3, 5 and 7 FT cycles, respectively (Table 1). Although the density more than doubled after 7 FT cycles, the pore volume only slightly decreased from 99.5% to 98.8%, affirming all aerogels to be super lightweight and highly porous. The ultra low density of 8 mg cm^{-3} is approximately equal to that of carbon nanotube sponges (5–10 mg cm^{-3}),[50,51] and is only two to nearly three times that of the lightest carbon nanotube (4 mg cm^{-3})[52] and silica (2–3 mg cm^{-3})[36] aerogels ever reported. These CNF aerogels are, however, clearly superior from the sustainable perspective being derived from a green and simple freeze-drying process from naturally abundant cellulosic feedstock.

With the presence of numerous surface polar hydroxyls and carboxyls, all CNF aerogels are extremely hydrophilic and super water-absorbing. The 0 FT aerogel absorbed 37 g g^{-1} water, reaching only 29% of its water absorbing capacity and reflecting its less interconnected small pores from rapid freezing at extremely low temperature (−196 °C). Water absorption increased to a maximum of 104 g g^{-1} for the 0.5 FT aerogel or 84% of its water absorbing capacity, indicative of large (several hundred microns), isotropic shaped and more interconnected pores framed with thicker pore walls from freezing at −20 °C. The water absorption lowered slightly to 92 g g^{-1} for the 1 FT aerogel as pores became more irregular and were loosely attached to thin fibers emerging by thawing, then rapid freezing at −196 °C. A close examination of these stepwise rapid and slow freezing as well as thawing cycles on the development of aerogel morphologies and properties leads to the conclusion that slower freezing promotes a more extensive assembly of CNFs into interconnected porous structures and thus favors water absorption. Water absorption capacities continued to decrease to 86, 77 and 53 g g^{-1} for 3, 5 and 7 FT aerogels, respectively, as a result of their significantly increased density and slightly reduced aerogel volume. Based on the observed unchanged aerogel volume upon water saturation, water absorption capacities showed an inverse relationship with aerogel densities as expected from eqn (3) and a significant drop between 1 and 3 FT cycles (Table 1). The measured water absorption for 0.5 and 1 FT aerogels are 15 and 25%, respectively, below the calculated 123 g g^{-1} capacities, reflecting the inaccessibility of some pores. With increased FT cycles to 3 and above, the measured water absorption values are very close to the calculated values, indicating more interconnected pores that are accessible for water absorption despite reduced capacities with increasing FT cycles.

The BET nitrogen adsorption showed reversible adsorption and desorption loops absent of level off points at high relative pressures for both 0 and 3 FT aerogels (Fig. 5a), typical of type II adsorption isotherms for nonporous or macro-porous structures. The specific surface area and total pore volume of the 0 FT aerogel were 30.01 m^2 g^{-1} and 0.082 m^3 g^{-1} (inset, Fig. 5a), respectively. These relatively low values are consistent with the highly associated and ice crystal templated CNFs into film-like structures and, most significantly, the loss of the nano-scale dimensions of CNFs. After 1 FT cycle, the specific surface area and total pore volume decreased to 12.99 m^2 g^{-1} and 0.021 m^3 g^{-1}, respectively. The specific surface area remained similar after 3 FT cycles (12.72 m^2 g^{-1}) and slightly increased after 5 (14.99 m^2 g^{-1}) and 7 FT (13.98 m^2 g^{-1}) cycles. The total pore volume was also unchanged after 3 FT cycles (0.021 cm^3 g^{-1}) and increased after 5 FT cycles (0.025 cm^3 g^{-1}), but lowered after 7 FT cycles (0.017 cm^3 g^{-1}). Both the specific surface area and total pore volume of all 1–7 FT aerogels were significantly lower than those of the 0 FT aerogel, *i.e.*, to half to one quarter, again reflecting the highly assembled CNFs in slow freezing. While the 0 FT aerogel had nearly four times the pore volume and more than twice the specific surface area than those of the 3 FT aerogel, both contained mainly macro-pores with small quantities of meso-pores centered at 4 and 10 nm, respectively

Table 1 Density, porosity, and water absorption of CNF aerogels from different FT cycles

FT cycles		0	0.5	1	3	5	7
Density (mg cm^{-3})		8.0	8.1	8.1	11.6	12.9	18.7
Porosity (%)		99.5	99.5	99.5	99.3	99.2	98.8
Water absorption (g g^{-1})	Measured	36	104	92	86	77	56
	Calculated	124	123	123	86	77	53

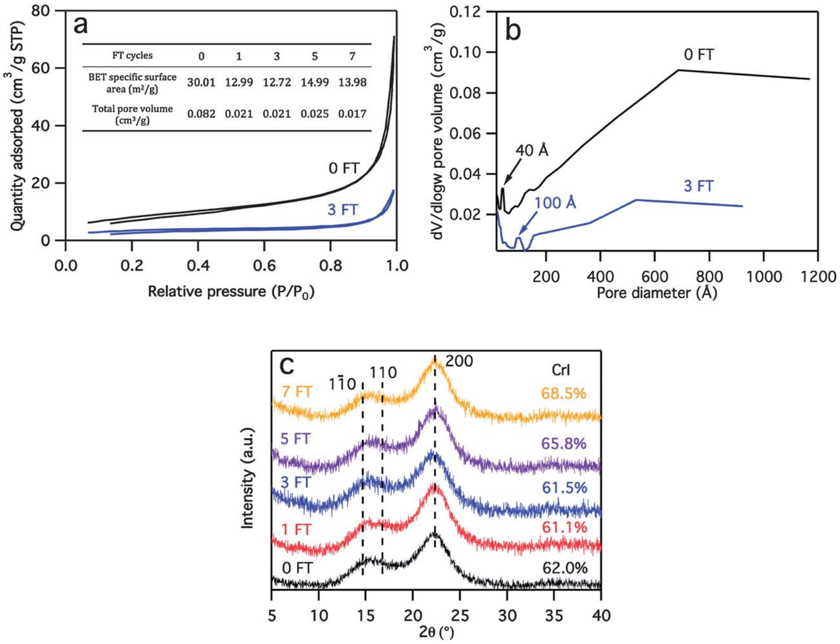

FT cycles	0	1	3	5	7
BET specific surface area (m²/g)	30.01	12.99	12.72	14.99	13.98
Total pore volume (cm³/g)	0.082	0.021	0.021	0.025	0.017

Fig. 5 Pore and crystalline structures of CNF aerogels from different F–T cycles: (a) BET isotherm and (b) pore size distribution. (c) XRD spectrum and crystallinity (CrI). The inset in (a) shows the specific surface areas and total pore volume.

(Fig. 5b). The XRD spectrum showed typical cellulose Iβ structures for all CNF aerogels, with the peaks at $2\theta = 14.7°$, $16.8°$ and $22.7°$ (Fig. 5c) assigned to $1\bar{1}0$, 110, and 200 crystallographic planes of the monoclinic cellulose Iβ lattice, respectively.[53] CNF aerogels showed constant crystallinity values *ca.* 61–62% from 0 to 3 FT cycles, then increased to 65.8% and 68.5% after 5 and 7 FT cycles, respectively, consistent with their increased densities. The slight crystallization with 5 and 7 FT cycles gave further evidence to the improved CNF association.

Both BET and XRD results support ice templated freezing–thawing to be effective in concentrating and facilitating the assembly of cellulose nanofibrils into highly crystalline domains around ice crystals. Direct liquid nitrogen freezing generates small ice crystals that upon sublimation leave small pores among limited assembled CNFs, yielding aerogels with relative higher specific surface areas and pore volumes, but weak physical integrity and low water absorption capacity. On the other hand, stronger and more ordered association among CNFs could be induced by slowly freezing and thawing, leading to aerogels with more inter-connected pore structures, improved structural integrity and water absorption capacity and even increased crystallinity, but reduced specific surface areas and pore volumes.

High specific surface area CNF aerogels *via tert*-butanol exchange

As manifested in previous sections, enhanced CNF association from FT cycles could improve mechanical integrity; however at the expense of reduced specific surface area and pore volume. In an attempt to improve the specific surface area, water in the 3 FT hydrogel was exchanged with *tert*-butanol and then freeze-dried to yield the 3 FTTBA aerogel. The 3 FTTBA aerogel appeared similar to the 3 FT aerogel, but had a significantly improved water absorption capacity of 116 g g^{-1}, approximately 35% higher than 86 g g^{-1} of the 3 FT aerogel. Cross-sectional SEM images of the 3 FTTBA aerogel showed macro-porous structures (Fig. 6a) as the 3 FT aerogel (Fig. 3g). Upon closer inspection, the pore walls of the 3 FTTBA aerogel revealed numerous smaller pores with diameters ranging from tens of nanometers to microns (Fig. 6b), in significant contrast to the smooth and intact pore walls of the 3 FT aerogel (Fig. 3g), and to which the increased water absorption is attributed. Besides, the previously observed thin fibers on pore wall films before solvent exchange (Fig. 3g and h) were no longer discernible on the pore wall surface (Fig. 6b). The external surface of the 3 FTTBA aerogel also contained numerous small nanometer- and micrometer-sized pores, as well as ultrathin nanofibrils (Fig. S5†).

The BET nitrogen adsorption–desorption of the 3 FTTBA aerogel showed a typical type IV isotherm that leveled off at high relative pressure (Fig. 6c), also in contrast to the 3 FT aerogel (Fig. 5a). The isotherm exhibited a narrow hysteresis loop with almost vertical and nearly parallel type H1 adsorption and desorption branches, indicating the presence of narrowly distributed uniform cylindrical meso-pores. The exchange with *tert*-butanol significantly increased the specific area, showing a 9 fold increase from 12.7 m^2 g^{-1} of the 3 FT aerogel to 117.8 m^2 g^{-1} of the 3 FTTBA aerogel (inset, Fig. 6c). Besides, the total pore volume increased over 47 times from 0.021 cm^3 g^{-1} to 1.16 cm^3 g^{-1}. The pore size distribution curve obtained from the desorption branch showed a bimodal distribution of a small peak between 2–7 nm and a major peak between 20–90 nm, confirming the coexistence of meso- and macro-pores and consistent with the SEM observation (Fig. 6d). BET results confirmed that exchanging water with *tert*-butanol led to a

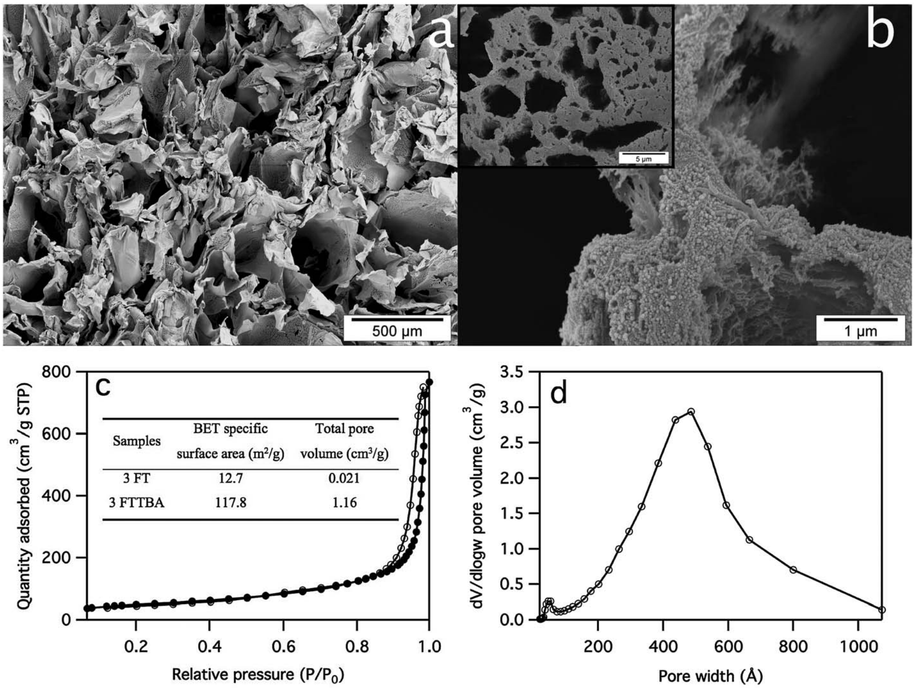

Samples	BET specific surface area (m²/g)	Total pore volume (cm³/g)
3 FT	12.7	0.021
3 FTTBA	117.8	1.16

Fig. 6 3 FTTBA aerogels: (a and b) SEM images of radial cross-sections; (c) specific surface area; (d) pore size distribution. The inset in (c) shows the specific surface area and total pore volume of 3 FT and 3 FTTBA aerogels.

much higher specific surface area and pore volume due to the generation of numerous meso-pores. In solvent exchange, both free and bound water on CNFs are replaced with *tert*-butanol, which contains only one hydroxyl to hydrogen bond with surface hydroxyls and carboxyls of assembled CNFs, to provide the bulky *tert*-butyl groups for steric hindrance to prevent CNFs from self-assembly, leaving interfibrillar meso- and macro-pores. Such hierarchical porous structures of CNF aerogels, *i.e.*, inter-CNF meso- and macro-pores ranging from 2 to 90 nm as well as macroscopic open cell pores of several hundred microns in size, have not been previously reported. These unique CNF aerogels could be used to design materials with superior mass transport while allowing diffusion of small active ingredients.

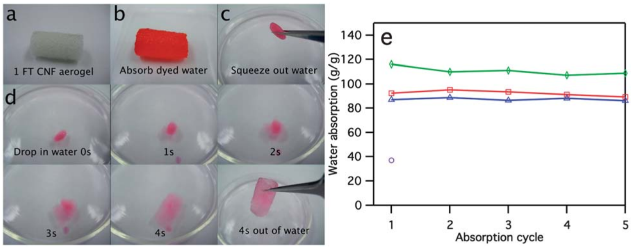

Fig. 7 1 FT CNF aerogel: (a) as is in air, (b) saturated with water colored with Procion red dye, (c) finger-squeezed dried from (b), (d) sequential snapshots of (c) reabsorbing water to full shape recovery in 4 s as labeled, and (e) cyclic water absorption (squeezed dried in between cycles) of (○) 0 FT; (□) 1 FT; (Δ) 3 FT; (◇) 3 FTTBA aerogels.

Shape recovery and cyclic desorption–absorption of CNF aerogels

With interconnected macro-porous structures and physical integrity, 1 FT CNF aerogels showed superior water absorption and were further observed for shape recovery properties (Fig. 7a). When immersed in water (colored with Procion red dye for clarity), CNF aerogels rapidly absorbed water at around 100 times their own weight without noticeable changes in the volume or shape. Over 90% of absorbed water could be easily removed by hand squeezing the CNF aerogel into a compact ball that could reabsorb water instantaneously and return to the original size and shape in 4 s, showing excellent water-activated shape recovery (Video in the ESI†). Reusability of aerogels was tested after cyclic hand squeezing–reabsorption. Both 1 and 3 FT aerogels showed great reusability without losing water absorption capacities during five repeated cycles (Fig. 7b). The 1 FT aerogel absorbed approximately 5% more water after the first reabsorption, possibly due to slight deformation of the thinner pore walls and more irregularly sized pores. The 3 FTTBA aerogel also demonstrated great squeezing–reabsorption reusability over five cycles. All FT CNF aerogels exhibited excellent wet strength and shape retention, *i.e.*, withstanding hand squeezing without breaking or falling apart even after over 20 cycles. None of the aerogels showed noticeable expansion upon absorption and the absorbed water could be easily squeezed out, indicating that the absorbed water mainly filled in the open pores. It should be noted that the 0 FT CNF aerogel turned paste like and broke apart upon gentle squeezing; therefore could not be reused, further attested to the aerogel microstructure formation from ice templating by slower freezing at −20 °C. These ice templated CNF aerogels from freezing–thawing not only recover much faster than thermoset polyamide–epichlorohydrin resin cross-linked cellulose nanofibril/microfibril aerogels (10 s),[30] but also show strong structural integrity without the need for chemical crosslinking.

Conclusions

This work has shown the significance of freezing at −20 °C as well as cyclic freezing (−20 °C, 15 h) and thawing (room temperature, 9 h) in forming hydrogels from TEMPO oxidized cellulose nanofibrils (CNFs), then aerogels by freeze-drying. Freezing induced self-assembling of CNFs and ice nucleation at a slow rate are key to the structural integrity and properties of CNF hydrogels and aerogels. Freezing at −20 °C allows slower super-cooling of CNF suspensions to concentrate CNFs into more orderly assembled crystalline domains and slower nucleation of ice crystals to grow in size, upon sublimation, leaving pores more than 20 times of those from rapid super-cooling at −196 °C. The common practice of freezing in liquid nitrogen (−196 °C) produces numerous small ice crystals that limit CNF association or gelation and, upon freeze-drying, form aerogels containing smaller 10–30 micron pores surrounded by loosely associated thin walls with very weak structural integrity and low water absorption. The assembly of CNFs by cyclic freezing–thawing is apparent at concentrations as low as 0.05%, but only leads to aerogels with more ordered pore structures and thicker film-like pore walls at and above 0.2% threshold concentration. The as-formed aerogels are structurally robust with large pores that are over several hundred microns in size, extremely low densities of 8.0 mg cm^{-3} and ultra-high porosity of 99.5% and high water absorption capacity of 104 g g^{-1}. Increasing numbers of freezing–thawing cycles induce further CNF association as manifested by the increased aerogel density (from 8.1 to 18.7 g cm^{-3}) and crystallinity (from 61 to 68.5%), but reduced pore sizes or lowered water absorption (92 to 53 g g^{-1}). Exchanging water in 3 FT hydrogel with *tert*-butanol followed by freeze-drying produced even more superior CNF aerogels with more than 5 times the pore volume (1.19 m^3 g^{-1}) and 10% higher water absorption (116 g g^{-1}) and, most significantly, nearly 10 times the specific surface area (117.8 m^2 g^{-1}) in hierarchical interconnected porous structures of ordered macroscopic pores of several hundred microns wide, as well as inter-CNF meso- and macro-pores ranging from 2 to 90 nm. All CNF aerogels are super water-absorbing and retain excellent physical integrity in water, demonstrating full and repetitive shape recovery in 4 s in hand squeezing–reabsorption for at least 20 cycles. This superior wet resilience and reusability could be ascribed to the highly crystalline cellulose nanofibrils and strong associations as induced by ice-crystal templating that is unmatched by amorphous aerogels from dissolved cellulose or uncrosslinked nanocellulose. To the best of our knowledge, this is the first report on self-assembled CNF aerogels with superior wet resilience and water-activated shape recovery without chemical crosslinking.

Acknowledgements

Financial support for this research from the California Rice Research Board (Project RU-9) is greatly appreciated.

Notes and references

1 H. D. Gesser and P. C. Goswami, *Chem. Rev.*, 1989, **89**, 765–788.

2 A. C. Pierre and G. M. Pajonk, *Chem. Rev.*, 2002, **102**, 4243–4265.

3 R. W. Pekala, *J. Mater. Sci.*, 1989, **24**, 3221–3227.

4 H. Sehaqui, M. Salajkova, Q. Zhou and L. A. Berglund, *Soft Matter*, 2010, **6**, 1824–1832.

5 C. B. Tan, B. M. Fung, J. K. Newman and C. Vu, *Adv. Mater.*, 2001, **13**, 644–646.

6 J. Cai, S. L. Liu, J. Feng, S. Kimura, M. Wada, S. Kuga and L. N. Zhang, *Angew. Chem., Int. Ed.*, 2012, **51**, 2076–2079.

7 M. Paakko, J. Vapaavuori, R. Silvennoinen, H. Kosonen, M. Ankerfors, T. Lindstrom, L. A. Berglund and O. Ikkala, *Soft Matter*, 2008, **4**, 2492–2499.

8 A. J. Svagan, M. Samir and L. A. Berglund, *Adv. Mater.*, 2008, **20**, 1261–1269.

9 R. T. Olsson, M. Samir, G. Salazar-Alvarez, L. Belova, V. Strom, L. A. Berglund, O. Ikkala, J. Nogues and U. W. Gedde, *Nat. Nanotechnol.*, 2010, **5**, 584–588.

10 H. Jin, M. Kettunen, A. Laiho, H. Pynnonen, J. Paltakari, A. Marmur, O. Ikkala and R. H. A. Ras, *Langmuir*, 2011, **27**, 1930–1934.

11 C. Aulin, J. Netrval, L. Wagberg and T. Lindstrom, *Soft Matter*, 2010, **6**, 3298–3305.

12 J. T. Korhonen, M. Kettunen, R. H. A. Ras and O. Ikkala, *ACS Appl. Mater. Interfaces*, 2011, **3**, 1813–1816.

13 N. T. Cervin, C. Aulin, P. T. Larsson and L. Wagberg, *Cellulose*, 2012, **19**, 401–410.

14 C. Gebald, J. A. Wurzbacher, P. Tingaut, T. Zimmermann and A. Steinfeld, *Environ. Sci. Technol.*, 2011, **45**, 9101–9108.

15 M. Kettunen, R. J. Silvennoinen, N. Houbenov, A. Nykanen, J. Ruokolainen, J. Sainio, V. Pore, M. Kemell, M. Ankerfors, T. Lindstrom, M. Ritala, R. H. A. Ras and O. Ikkala, *Adv. Funct. Mater.*, 2011, **21**, 510–517.

16 J. T. Korhonen, P. Hiekkataipale, J. Malm, M. Karppinen, O. Ikkala and R. H. A. Ras, *ACS Nano*, 2011, **5**, 1967–1974.

17 J. Cai, S. Kimura, M. Wada and S. Kuga, *Biomacromolecules*, 2009, **10**, 87–94.

18 J. Cai, S. Kimura, M. Wada, S. Kuga and L. Zhang, *ChemSusChem*, 2008, **1**, 149–154.

19 H. Jin, Y. Nishiyama, M. Wada and S. Kuga, *Colloids Surf., A*, 2004, **240**, 63–67.

20 J. Innerlohinger, H. K. Weber and G. Kraft, *Macromol. Symp.*, 2006, **244**, 126–135.

21 F. Liebner, E. Haimer, A. Potthast, D. Loidl, S. Tschegg, M. A. Neouze, M. Wendland and T. Rosenau, *Holzforschung*, 2009, **63**, 3–11.

22 R. Gavillon and T. Budtova, *Biomacromolecules*, 2008, **9**, 269–277.

23 B. J. C. Duchemin, M. P. Staiger, N. Tucker and R. H. Newman, *J. Appl. Polym. Sci.*, 2010, **115**, 216–221.

24 Z. G. Wang, S. L. Liu, Y. Matsumoto and S. Kuga, *Cellulose*, 2012, **19**, 393–399.

25 R. Sescousse, R. Gavillon and T. Budtova, *Carbohydr. Polym.*, 2011, **83**, 1766–1774.

26 T. Saito, T. Uematsu, S. Kimura, T. Enomae and A. Isogai, *Soft Matter*, 2011, **7**, 8804–8809.

27 F. Jiang and Y.-L. Hsieh, 2013, in review.

28 H. Sehaqui, Q. Zhou and L. A. Berglund, *Compos. Sci. Technol.*, 2011, **71**, 1593–1599.

29 W. Zhang, Y. Zhang, C. H. Lu and Y. L. Deng, *J. Mater. Chem.*, 2012, **22**, 11642–11650.

30 L. Heath and W. Thielemans, *Green Chem.*, 2010, **12**, 1448–1453.

31 F. Jiang and Y.-L. Hsieh, *Carbohydr. Polym.*, 2013, **95**, 32–40.

32 W. S. Chen, H. P. Yu, Q. Li, Y. X. Liu and J. Li, *Soft Matter*, 2011, **7**, 10360–10368.

33 J. Lee and Y. L. Deng, *Soft Matter*, 2011, **7**, 6034–6040.

34 P. Lu and Y. L. Hsieh, *Carbohydr. Polym.*, 2012, **87**, 564–573.

35 P. B. Sarawade, J. K. Kim, H. K. Kim and H. T. Kim, *Appl. Surf. Sci.*, 2007, **254**, 574–579.

36 T. M. Tillotson and L. W. Hrubesh, *J. Non-Cryst. Solids*, 1992, **145**, 44–50.

37 H. Dong, F. J. Snyder, S. K. Williams and W. J. Andzelm, *Biomacromolecules*, 2013, **14**, 3338–3345.

38 A. Dorris and D. G. Gray, *Cellulose*, 2012, **14**, 3338–3345.

39 F. Yokoyama, I. Masada, K. Shimamura, T. Ikawa and K. Monobe, *Colloid Polym. Sci.*, 1986, **264**, 595–601.

40 T. Abitbol, T. Johnstone, T. M. Quinn and D. G. Gray, *Soft Matter*, 2011, **7**, 2373–2379.

41 Y. X. Wang, C. Y. Chang and L. N. Zhang, *Macromol. Mater. Eng.*, 2010, **295**, 137–145.

42 J. Li, Y. Lu, D. J. Yang, Q. F. Sun, Y. X. Liu and H. J. Zhao, *Biomacromolecules*, 2011, **12**, 1860–1867.

43 Y. Lu, Q. F. Sun, D. J. Yang, X. L. She, X. D. Yao, G. S. Zhu, Y. X. Liu, H. J. Zhao and J. Li, *J. Mater. Chem.*, 2012, **22**, 13548–13557.

44 *Polymer Handbook*, ed. J. Ganster and H. P. Fink, Wiley & Sons, New York, 1999.

45 D. R. Lide, *CRC Handbook of Chemistry and Physics (Internet Version)*, CRC Press, Boca Raton, FL, 2011.

46 L. Segal, J. J. Creely, A. E. Martin, Jr and C. M. Conrad, *Text. Res. J.*, 1959, **29**, 786–794.

47 F. Jiang, S. Han and Y.-L. Hsieh, *RSC Adv.*, 2013, **3**, 12366–12375.

48 K. E. Zachariassen and E. Kristiansen, *Cryobiology*, 2000, **41**, 257–279.

49 J. Q. Han, C. J. Zhou, Y. Q. Wu, F. Y. Liu and Q. L. Wu, *Biomacromolecules*, 2013, **14**, 1529–1540.

50 X. C. Gui, J. Q. Wei, K. L. Wang, A. Y. Cao, H. W. Zhu, Y. Jia, Q. K. Shu and D. H. Wu, *Adv. Mater.*, 2010, **22**, 617–621.

51 M. B. Bryning, D. E. Milkie, M. F. Islam, L. A. Hough, J. M. Kikkawa and A. G. Yodh, *Adv. Mater.*, 2007, **19**, 661–664.

52 J. H. Zou, J. H. Liu, A. S. Karakoti, A. Kumar, D. Joung, Q. A. Li, S. I. Khondaker, S. Seal and L. Zhai, *ACS Nano*, 2010, **4**, 7293–7302.

53 F. Jiang, A. R. Esker and M. Roman, *Langmuir*, 2010, **26**, 17919–17925.